On the trade-off between enhancement of the spatial resolution and noise amplification in conical-scanning microwave radiometers

Matteo Alparone, *Member, IEEE,* Ferdinando Nunziata, *Senior Member, IEEE,* Claudio Estatico, Adriano Camps, *Fellow, IEEE,* Hyuk Park, *Senior Member, IEEE,* and Maurizio Migliaccio, *Fellow, IEEE*

Abstract—The ability to enhance the spatial resolution of measurements collected by a conical-scanning microwave radiometer is discussed in terms of noise amplification and improvement of the spatial resolution. Simulated (and actual brightness temperature profiles) are analyzed at variance of different intrinsic spatial resolutions and adjacent beams overlapping. The actual measurements refer to Special Sensor Microwave Imager (SSM/I) data collected using the 19.35 GHz and the 37.00 GHz channels that matches the simulated configurations. The reconstruction of the brightness profile at enhanced spatial resolution is performed using an iterative gradient method which is specialized to allow a fine tuning of the level of regularization. Objective metrics are introduced to quantify the enhancement of the spatial resolution and noise amplification.

Numerical experiments show that the regularized deconvolution results in negligible advantages when dealing with low-overlapping/fine-spatial-resolution configurations. Regularization is a mandatory step when addressing the high-overlapping/low-spatial-resolution case and the spatial resolution can be enhanced up to 2.34 with a noise amplification equal to 1.56. A more stringent requirement on the noise amplification (up to 0.6) results in an improvement of the spatial resolution up to 1.64.

Index Terms—Resolution enhancement, inverse problem, deconvolution, microwave radiometer, conical scan, multi-channel data fusion.

I. INTRODUCTION

Microwave radiometers (MWRs) for Earth Observation (EO) are sensors that measure the emission of the Earth [1]. In a conventional scanning radiometer, a rotating antenna scans the scene, providing an output as function of the scan angle. The measured power depends on the system's parameters (e.g., receiver gain and noise figure, noise bandwith, antenna pattern, etc.), the apparent brightness temperature T_B and the brightness temperature coming from different directions. Assuming a well-calibrated measurement [2], the t-th radiometer

M. Alparone, F. Nunziata and M. Migliaccio are with the Dipartimento di Ingegneria, Università degli Studi di Napoli Parthenope, 80143 Napoli, Italy (e-mail: matteo.alparone@uniparthenope.it; ferdinando.nunziata@uniparthenope.it; maurizio.migliaccio@uniparthenope.it).

C. Estatico is with the Dipartimento di Matematica, Università degli Studi di Genova, 16146 Genova, Italy (e-mail: estatico@dima.unige.it). The work of Claudio Estatico is partially supported by GNCS-INDAM, Italy

A. Camps is with CommSensLab-María de Maeztu Unit, Universitat Politècnica de Catalunya-BarcelonaTech and IEEC/UPC, 08034 Barcelona, Spain

H. Park is with CommSensLab, Unidad María de Maetzu, also with the Department of Signal Theory and Communications, IEEC/CTE-UPC, Universitat Politécnica de Catalunya (UPC), 08034 Barcelona, Spain, and also with the Department of Physics, Castelldefels School of Telecommunications and Aerospace Engineering, UPC-BarcelonaTech, 08034 Barcelona, Spain.

measurement can be written as [3]:

$$b_t = \int_\Omega A(\rho) T_B(\rho) d\rho \tag{1}$$

where ρ is the integration variable spanning the spatial domain Ω and $A(\cdot)$ is the measurement response function (MRF) [2] of the microwave radiometer, i.e., a smooth function that weights the brightness temperature $T_B(\rho)$ with the antenna pattern. However, since the signal received by the MWR is integrated over a short period to reduce the measurement variance and because of the rotation of the scanning antenna during the integration period, $A(\cdot)$ is actually a smeared version of the projected antenna pattern [2], [4], [5]. MWR observations are typically provided into two formats: swath data (that preserve the native scan geometry); gridded data (that are organised into an image format with annotated geolocation information) [6]. There is an increasing interest towards gridded products since they allow observing the time variability of geophysical parameters at fixed locations [7]–[10]. Gridded products are obtained by swath-based measurements using interpolation methods that call for a trade-off between noise amplification and improved spatial resolution. The simplest approach consists of using interpolation schemes that result in low-noise and low-resolution gridded products [11]–[13]. However, there is a growing interest towards finer spatial resolution products for new regional-scale MWR applications. Within this context, methods to grid radiometer products on a spatial scale finer than the -3 dB area of the radiometer MRF have been proposed in the literature. Those approaches, which are basically antenna pattern deconvolution methods, enhance the spatial resolution of the radiometer measurements by solving a linear inverse problem [14]. Several algorithms have been proposed that are based on either direct inversion of the linear ill-conditioned problem [4], [5], [15] or by using iterative methods [5], [16]–[19]. The latter are to be preferred when addressing large-scale problems such as the one resulting from the enhancement of the spatial resolution of microwave radiometer measurements [18]. The achieved spatial resolution depends on the MRF, and the reconstruction method itself. In the case of iterative regularization methods, the convergence rate can be relatively slow and, therefore, methods to speed up this convergence rate have been proposed [20], [21]. The enhancement of the spatial resolution is limited by the overlapping of the radiometer measurements and depends on the sampling pattern. In addition, since noisier products are

obtained, a trade-off between the enhancement of the spatial resolution and the noise amplification must be considered [22]. In [23] the reconstruction performance of several deconvolution methods is discussed in terms of the achieved spatial resolution and noise amplification by subjectively stopping the iterations in each method.

In this study, a theoretical framework to discuss the performance of spatial resolution enhancement with respect to the intrinsic radiometer spatial resolution and the level of overlapping among adjacent beams is proposed. The theoretical framework is based on a preconditioned version of the gradient iterative regularization method (LW-P) that, originally developed in [21] to speed-up the convergence rate of the Landweber (LW) iterative method, is here specialized to tune the level of regularization by a proper setting of its parameters. This analyses are accomplished on both radiometer measurements, simulated using three MRFs that mimic three conical scanning radiometer's measurement configurations, and using actual radiometer measurements calling for different spatial resolutions and overlapping among adjacent beams.

The main novelties can be summarized as follows: a) for large-scale discretized MRF, it is theoretically shown that the coarser is the spatial resolution of the MWR, the larger is the instability of the linear system to be inverted. This has a direct implication on the regularizing capabilities of the deconvolution schemes to be applied; b) the preconditioned regularizing scheme is analyzed to provide a better understanding of its capability to filter high-frequency components and, therefore, to trade off regularization and enhancement capabilities; c) a quantitative analysis of reconstruction's performance is carried on by jointly accounting for regularization, enhancement capabilities and noise amplification.

The remainder of the paper is organised as follows. The spectral properties of the discretized MRF, and the regularization scheme that deconvolves the antenna pattern are discussed for different MWR configurations in Section II. Numerical experiments performed on both simulated and actual brightness profiles are discussed in Section III, and the conclusions are drawn in Section IV.

II. THEORETICAL BACKGROUND

In this section, a simplified 1D MRF is used to model the MWR measurement process in eq. (1), and to characterize the spectral properties of the discretized MRF for three MWR measurements configurations calling for different footprint sizes and degree of overlapping among adjacent beams. In addition, a regularizing scheme that exploits the spectral properties of the discretized MRF to control noise amplification in the reconstructed brightness profile is also presented.

A. Spectral analysis of the discretized MRF

From a physical viewpoint, the enhancement of the radiometer spatial resolution is possible since MWR makes multiple observations of the same scene under different viewing angles. Hence, coarse, but partially correlated measurements are available. A shift-invariant convolution with a Gaussian kernel is here used to model the MWR measurement process in the cross-track direction. Hence, the discretized version of eq. (1) leads to an underdetermined linear system of equations:

$$\mathbf{A}\mathbf{x} = \mathbf{b}\,, \qquad (2)$$

with $\mathbf{b} \in \mathbb{R}^m$ and $\mathbf{x} \in \mathbb{R}^n$ representing the m measurements and the n points where the finer spatial resolution brightness temperatures are to be reconstructed and $\mathbf{A}$ contains the discretized MRF. The retrieval of the brightness temperatures on the finer resolution grid is based on a suitable methodology to invert the highly under-determined ($m \ll n$) linear system (2). In addition, since the system comes from an ill-posed continuous problem, i.e. the Fredholm equation of the first kind with a smooth kernel (eq. (1)), the linear system (2) is also ill-conditioned. This means that the noise on the measurements significantly affects the spatial resolution enhancement process by limiting the quality of the reconstruction. Hence, regularizing schemes are mandatory to reconstruct the brightness temperature profile.

From a mathematical viewpoint, the challenges when inverting (2) depend on the $\mathbf{A}$ matrix. Hence, its special properties are here analysed. The entries of the $\mathbf{A}$ matrix are here modeled as follows [20]:

$$A_{i,j} = a_{\lfloor ig \rfloor - j}, \text{ for } i = 0, \dots, m-1 \\ \text{ and } j = 0, \dots, n-1 \quad, \qquad (3)$$

where $g = n/m > 1$, $\lfloor \cdot \rfloor$ is the floor function, and the entries of the (Gaussian kernel) vector a are given by

$$a_k = \exp(-k^2/2\sigma^2), \quad \text{for } k = -n+1, \dots, n-1\,. \qquad (4)$$

The standard deviation $\sigma > 0$ is a parameter which depends on the considered radiometer channel and is set in such a way that the -3dB width of the discretized MRF matches the MWR field of view. The coarser is the spatial resolution (the larger is σ) and the larger is the overlapping among adjacent beams, i.e., the available measurements are highly correlated.

To link σ to the stability of the linear system (2) to be inverted, a spectral analysis is carried on the $\mathbf{A}$ matrix that can be considered as the leading principal (i.e., upper-left) $m \times n$ submatrix of the square g-Toeplitz matrix $\mathbf{T} \in \mathbb{R}^{n \times n}$ [24] whose entries are defined as

$$T_{i,j} = a_{\lfloor ig \rfloor - j}, \quad \text{for } i, j = 0, \dots, n-1\,. \qquad (5)$$

In the context of spatial resolution enhancement, n is typically a large value, hence it can be shown [25] that the singular values s_k, for $k = 1, \dots n$, of $\mathbf{T}$ in eq. (5) are distributed as the inverse Fourier transform of the continuous extension of the Gaussian convolution kernel, that is:

$$s_{k+1} \approx b\sigma \exp(-c\sigma^2 k^2)\,, \quad \text{for } k = 0, n-1\,, \qquad (6)$$

where the constants $b, c > 0$ depend only on the dimension n. Moreover, all the m singular values of the $m \times n$ matrix $\mathbf{A}$ are well approximated by the first m singular values of $\mathbf{T}$, which leads to the following estimate of its 2-norm condition number

$$\mu_2(A) = s_1/s_m \approx \exp(b\sigma^2 m^2) = C^{\sigma^2}\,, \qquad (7)$$

where $C = \exp(bm^2) > 1$ does not depend on σ. This implies that, since $C^{\sigma_1^2} > C^{\sigma_2^2}$ with $\sigma_1 > \sigma_2$, for a fixed spatial

sampling (i.e., for a fixed pair (m,n)), the larger is σ the larger is the condition number of the matrix. Recalling that the latter gives information on the stability of the associated linear system, that is, how sensitive the solution $\mathbf{x}$ is to changes or errors in the measurements data $\mathbf{b}$ of eq. (2), the larger is σ (i.e., the coarser is the spatial resolution of the MWR channel) the larger is the conditioning number of the linear discrete system (eq. (2)) to be inverted to retrieve the brightness temperature on a finer spatial resolution grid.

B. Regularizing preconditioner

According to eq. (7), regularization is a mandatory step to reconstruct the brightness temperature on a finer spatial resolution grid. In this subsection, we first recall the conventional gradient-like LW regularization scheme [16] and then we review its preconditioned version (LW-P) that was developed in [21] to improve the convergence rate of the LW method. Finally, the regularizing properties of the preconditioner are here analyzed to design a regularizing scheme where the amount of regularization can be explicitly tuned. This is a mandatory step to provide a theoretical framework when jointly discussing enhancement capabilities with respect to noise amplification and regularization needed.

The LW method, also known as the gradient method with constant step size, minimizes the leas square functional:

$$\Omega_2(\mathbf{x}) = \frac{1}{2}\|A\mathbf{x} - \mathbf{b}\|^2 \qquad (8)$$

by means of the following iterative scheme:

$$\mathbf{x}_k = \mathbf{x}_{k-1} - \lambda \nabla \Omega_2(\mathbf{x}_{k-1}) \ , \qquad (9)$$

where $\lambda \in (0, 2/\|A\|^2)$ is the step-size of the iterative method. By straightforward computation of the gradient, eq. (9) can be rewritten as

$$\mathbf{x}_k = \mathbf{x}_{k-1} - \lambda \mathbf{A}^*(\mathbf{A}\mathbf{x}_{k-1} - \mathbf{b}) \ , \qquad (10)$$

being $\mathbf{A}^* \in \mathbb{R}^{n \times m}$ the adjoint operator of $\mathbf{A}$, that is, the transpose matrix in our real case. In the noiseless case, the iteration converges to the generalized inverse $\mathbf{x}^\dagger \in N(\mathbf{A})^\perp$ for $\mathbf{x}_0 = 0$, or $\mathbf{x}^\dagger + \mathbf{x}_0'$ for $\mathbf{x}_0 \neq 0$, where $\mathbf{x}_0'$ is the orthogonal projection of the initial guess $\mathbf{x}_0$ onto the null space $N(\mathbf{A})$. In the noisy case, the method belongs to the family of iterative regularization algorithms, where an early stop of the iterations acts as regularization parameter.

Iterative methods often result in a low convergence rate [3]. In [21] a LW-P method is proposed to improve the LW convergence rate by exploiting the structured nature of the $\mathbf{A}$ matrix using a preconditioner. A regularizing preconditioner is the operator P_f [26], [27] that, applied to the linear system (2), allows for a clustering at unity of the singular values related to the signal subspace only. The preconditioner is a filtered version of the well studied Strang straightforward circulant preconditioner [28], which is hereinafter briefly described. The algebra of circulant matrices allows for fast, i.e. $O(n \log n)$, matrix-vector inversion and computation of the spectrum via FFT. Anyway, in general, given a $n \times n$ Toeplitz matrix $\tilde{T}_{i,j} = a_{i-j}$ for $i, j = 0, \ldots, n-1$, the Strang circulant preconditioner $S = S(\tilde{\mathbf{T}})$ of the matrix $\tilde{\mathbf{T}}$ is defined by simple

arrangements of its central elements, that is, by copying the central diagonals of $\tilde{T}$ and reversing them to complete the circulant structure as follows:

$$S_{i,j} = s_{i-j} = \begin{cases} a_{i-j} & |i-j| \leq \lfloor n/2 \rfloor \\ s_{n-(i-j)} & \text{otherwise} \end{cases} . \qquad (11)$$

In [27] it was shown that a large part of the eigenvalues of the preconditioned matrix $S^{-1}\tilde{\mathbf{T}}$ clusters at unity, that is $S^{-1}\tilde{\mathbf{T}} \approx \mathbf{I}$, since the identity matrix has all the eigenvalues equal to 1. This property can be explained by recalling that the central diagonals of any Toeplitz matrix correspond to the central values of the associated convolution kernel, which usually keep the most important information on the point spread function (remember that convolution kernels usually vanish far from the central points).

In this study, to ensure regularization (i.e., to obtain a regularizing preconditioner) we require for a clustering at unity of the spectrum of the preconditioned matrix in the signal space only, in order to avoid, in the spatial enhancement process, the amplification of the components mainly corrupted by noise. Hence, since the $n \times n$ symmetric matrix $\mathbf{A}^*\mathbf{A}$ is approximated by the $n \times n$ symmetric matrix $\tilde{\mathbf{T}}^*\tilde{\mathbf{T}} = \tilde{\mathbf{T}}^2$, the regularized version of the Strang preconditioner can be designed as follows. First, the spectral decomposition of (11) is considered:

$$S = S(\tilde{\mathbf{T}}\mathbf{T}) = F \operatorname{diag}(\lambda_1, \lambda_2, \ldots, \lambda_n)F^* , \qquad (12)$$

where $\lambda_i \geq 0$ are the eigenvalues corresponding to the eingevectors in the columns of the Fourier matrix $\mathbf{F}$, since S is a circulant matrix, and $\operatorname{diag}(v_1, \ldots, v_n)$ denotes the diagonal matrix with diagonal entries $v_1, \ldots, v_n$. Then, the inverse of the filtered preconditioner is directly computed as:

$$P_f^{-1} = \mathbf{F} \operatorname{diag}(f_\alpha(\lambda_1^2), f_\alpha(\lambda_2^2), \ldots, f_\alpha(\lambda_n^2))\mathbf{F}^* . \qquad (13)$$

In this study, the scalar real function

$$f_\alpha(x) = (x + \alpha)^{-1} , \qquad (14)$$

is considered to design the so-called "regularizing inverse", that is, a (family of) bounded function defined on $x \geq 0$ which approximates, for the regularization parameter $\alpha \to 0$, the unbounded inverse function x^{-1} defined on $x > 0$ only. Basically, a regularized inverse allows a "filtered" inversion. The idea behind the use of eq. (14) when inverting the system in eq. (13) is to reduce the amplification of the smallest eigenvalues of $\mathbf{S}^*\mathbf{S}$, i.e.; a phenomenon that arises when the straightforwardly inverting the linear system. This way, the regularized preconditioner P_f^{-1} is a filtered version of the inverse of $\mathbf{S}(\tilde{\mathbf{T}}^*\tilde{\mathbf{T}})$, so that $P_f^{-1}\tilde{\mathbf{T}}^*\tilde{\mathbf{T}} \approx P_f^{-1}\mathbf{A}^*\tilde{\mathbf{A}}$ fulfills the following heuristic rule [21],

$$P_f^{-1}\mathbf{A}^*\mathbf{A} \approx \begin{cases} \mathbf{I} & \text{in the signal subspace} \\ \mathbf{A}^*\mathbf{A} \approx 0 & \text{in the noise subspace} \end{cases} , \qquad (15)$$

where $\mathbf{I}$ is the identity matrix, so that the convergence is very fast in the signal subspace (where the preconditioned matrix is close to the identity, i.e., the system is already almost resolved), whilst is slow in the noise subspace (where the preconditioned matrix is vanishing). The signal subspace is

the vector subspace of the solution space $\mathbb{R}^n$ less sensitive to noise amplification in the enhancement procedure, and it is related to the large singular values of $\mathbf{A}$. On the contrary, the noise subspace is the vector subspace highly sensitive to noise amplification, related to the smallest (and vanishing to zero) singular values of $\mathbf{A}$. It must be recalled that, in any convolution model, the signal subspace is the low frequency subspace, while the noise subspace is the high frequency one. Indeed, the high frequency components are highly reduced by the convolution integral operator (i.e., multiplied by the smallest singular values), by virtue of the Riemann-Lebesgue Theorem. To better understand the concept of "filtered" inversion the following example can be considered. The difference between a non-filtered and a filtered preconditioner relies in the scalar real function used in computing the inverse of eq. (12), i.e. $f(x) = x^{-1}$ for the non-filtered and $f_\alpha(x) = (x + \alpha)^{-1}$ for the filtered cases, respectively. In our case $x = \lambda_i^2$ where λ_i are the eigenvectors of A and the square elevation is due to the term A^*A. Considering $\lambda_1 \gg \lambda_n$ (e.g. $\lambda_n = \lambda_1/10^4$) and the non-filtered preconditioner, it can be noted that the smaller eigenvalue is strongly amplified in the inversion (see Fig. 1(a)). In the filtered case, i.e., when using $f_\alpha(x)$, the amplification effect is strongly reduced (see Fig. 1(b)). This is due to the fact that the regularized inverse (11) causes a shifting of the hyperbole in Fig. 1(a) by a factor α towards the negative x-axis, avoiding the excessive amplification of the smaller eigenvalues. It is worth noting that the regularized inverse (14)
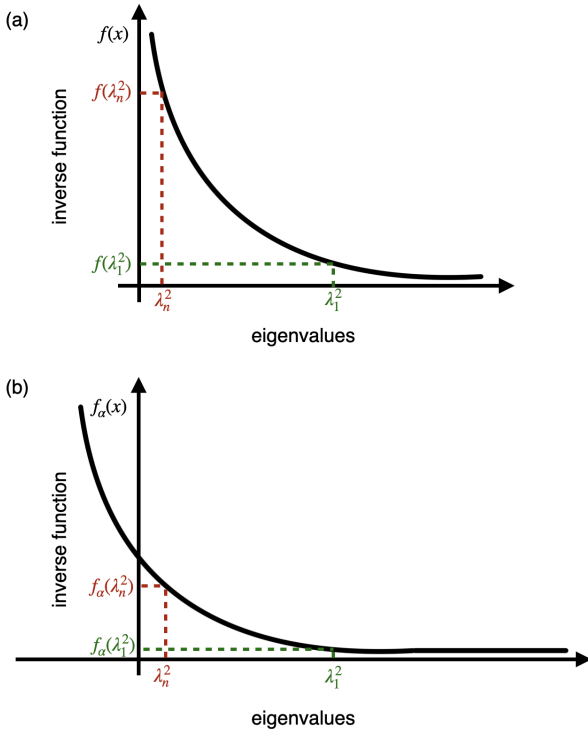

Fig. 1. Sketch of the scalar real functions used in computing the inverse of (12) for the (a) non-filtered, (b) filtered cases, respectively.

we used in this study is based on the conventional Tikhonov regularization filtering. Other low-pass filtering functions can

be also applied (see the filters in Section 3 of [29]), leading to different regularization behaviours.

Once the spectral properties of P_f and its filtering ability has been discussed, the k-iteration of the LW-P can be obtained starting from the least square preconditioned system

$$P_f^{-1}\mathbf{A}^*\mathbf{A}\mathbf{x} = P_f^{-1}\mathbf{A}^*\mathbf{b} \quad , \qquad (16)$$

whose set of solutions coincides with the set of solutions of the least square minimization problem of eq. (8), because of the invertibility of P_f. Hence, the k-th iteration of the LW-P method is very similar to eq. (10) and reads as

$$\mathbf{x}_k = \mathbf{x}_{k-1} - \lambda P_f^{-1}\mathbf{A}^*(\mathbf{A}\mathbf{x}_{k-1} - \mathbf{b}) \ . \qquad (17)$$

III. NUMERICAL EXPERIMENTS

In this section, thought numerical experiments are presented and discussed. The reconstruction problem is formulated according to eq. (2) where $n = 64$ and $m = 1400$ and reference is made to a realistic 1D microwave radiometer configuration that performs uniformly spaced (25 km) measurements over a 1400 km swath. This means that the brightness temperature profile is reconstructed on a finer grid whose spacing is 1 km. Noisy measurements $\mathbf{b} \in \mathbb{R}^m$ are obtained through the forward problem of eq. (2) where the rectangular matrix $\mathbf{A} \in \mathbb{R}^{m \times n}$ (with $m \ll n$) is built using a shift-invariant Gaussian-shaped function $G(\cdot)$. An additive white Gaussian noise (AWGN) with standard deviation is 1 K is considered and different $\mathbf{x} \in \mathbb{R}^n$ reference scenarios are used to showcase meaningful scenarios.

The brightness profile $\mathbf{x}$ is reconstructed using the LW-P method by a suitable choice of the α parameter in eq. (14). This means that α allows tuning the degree of regularization of the gradient-like method encompassing also the conventional LW.

To analyse the role played by the intrinsic MWR spatial resolution and the degree of overlapping among adjacent beams, three measurements configurations (MC) are used:

- MC1 refers to the low spatial resolution and high overlapping case, see Fig. 2 (a). In this case, the -3 dB width of MRF is equal to 43 km, and the percentage of overlapping among adjacent beams (PO) is equal to 77%.
- MC2 refers to an intermediate case, see Fig. 2 (b), where the -3 dB width of the MRF is equal to 34 km and PO is equal to 65%.
- MC3 refers to the finest spatial resolution and lowest overlapping case, see Fig. 2 (c), where the MRF calls for a 20 km width and PO is equal to 39%.

To discuss qualitatively and quantitatively reconstruction's performance, the following objective metrics are introduced:

- Improvement Factor (IF). It is defined as the ratio between the -3 dB width of the reconstructed and the measured pulse-like functions. It can assume values in the range $[1, \infty)$, and the larger IF is, the finer is the spatial resolution of the reconstructed profile.
- Peak-to-background Ratio (PBR). It is defined as the ratio between the brightness level measured over the top of a pulse-like reference profile with respect to the

reconstructed brightness level value. PBR = 1 stands for perfectly reconstructed brightness level; while PBR > 1(< 1) stands for overestimated (underestimated) reconstructions. Hence it allows quantifying over- and under-estimation that may result from the reconstruction of spot-like discontinuities, see Fig. 3.

- Depth-to-Null Ratio (DNR). It is defined as the ratio between the background brightness level measured over the reconstructed profile and the reference one. It is evaluated in the region enclosed by two pulse-like functions and it aims at quantifying the ability of the reconstruction method to recover abrupt discontinuities with a limited over-smoothing. DNR = 1 stands for a background perfectly reconstructed; while DNR > 1(< 1) stands for over- (under-)estimation, see Fig. 3.
- Noise amplification. The absolute value of the root mean square error (RMSE) between the measurement and the reconstructed field is evaluated over a homogeneous area to quantify the amplification of noise that comes with the resolution enhancement process.

The first set of experiments is related to simulated noisy measurements obtained using the three MCs depicted in Fig. 2. Then, experiments performed using profiles extracted from actual MWR measurements collected by the SSM/I are discussed.

A. Simulated measurements

The first experiment consists of discussing the enhancement of the spatial resolution by contrasting the point spreading function in the non-enhanced and enhanced cases. On this purpose, an unrealistic reference profile (RP) that consists of 1-pixel Kronecker function calling for a 10^6 K brightness temperature is used. The noisy measurements (linearly interpolated on the finer-resolution grid) are depicted together with the LW and LW-P reconstructions in Fig. 4. The LW-P is run with a low level of regularization, i.e., $\alpha = 5 \cdot 10^{-3}$ and the LW case, that is approximated by $\alpha = 5 \cdot 10^{-4}$, is also annotated for comparison purposes. To better visualise the outputs, the decibel (dB) scale is used. Figure 4 (a), (b) and (c) refer to the MC of Fig. 2 (a), (b) and (c), respectively. As expected, MC3 calls for the finest spatial resolution; while the coarsest one is achieved when using MC1. The reconstructions related to MC1 are depicted in Fig. 4 (a) where it can be noted that, although both LW and LW-P improve the spatial resolution with respect to the measurements, LW-P performs best since it results in the brightness level closest to the RP one. To quantitatively analyse the reconstruction's performance, the IF metric is evaluated (see Table I) confirming that LW-P (1.57) outperforms LW (1.09). This implies that a smaller level of regularization allows a better reconstruction of spot-like discontinuities since it reduces the over smoothing. Similar comments apply when dealing with the MC2 case, see Fig. 4 (c). In the MC3 case, LW performs better than LW-P. This is likely due to the finer resolution of MWR measurements, and the low overlapping among adjacent beams affecting the performance of LW-P. A deeper analysis on the three MC cases can be provided analysing the matrix system function
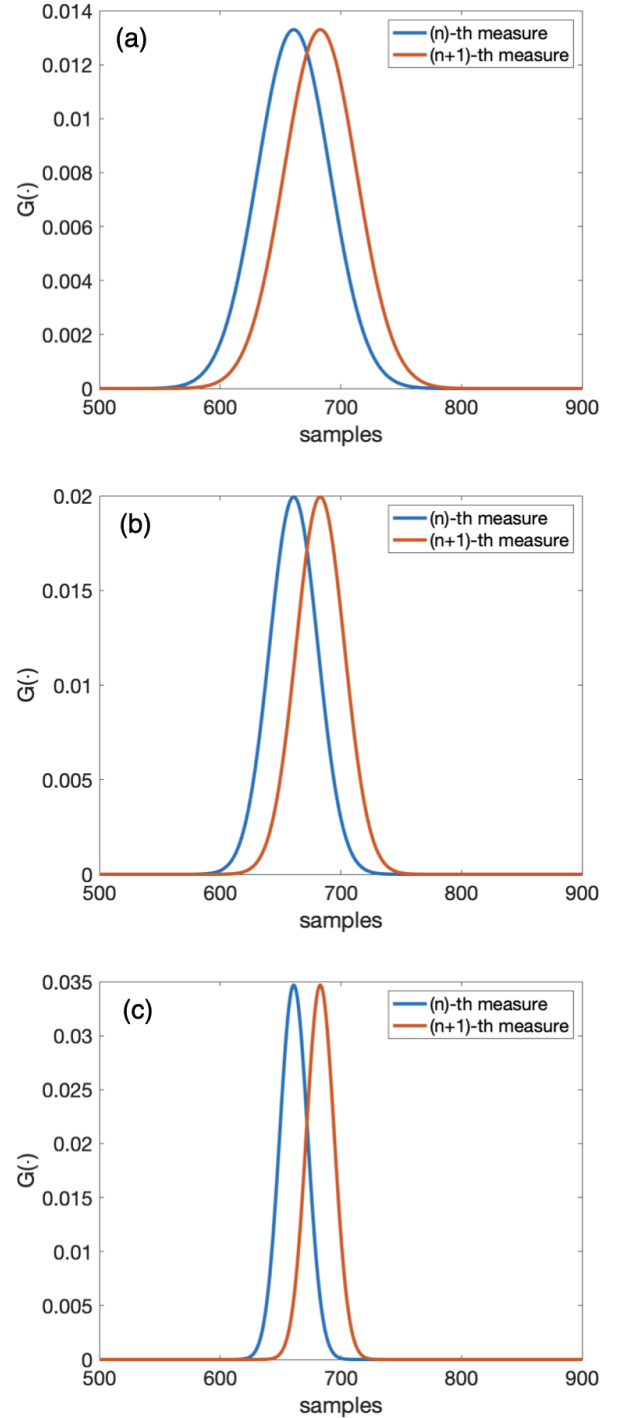

Fig. 2. System matrix A related to the three MCs. The $G(\cdot)$ functions belonging to the i-th row (restricted to the range 500 to 900 samples) and centered at the the n-th and (n+1) samples are here shown for the cases MC1 (a) MC2 (b) and MC3 (c).

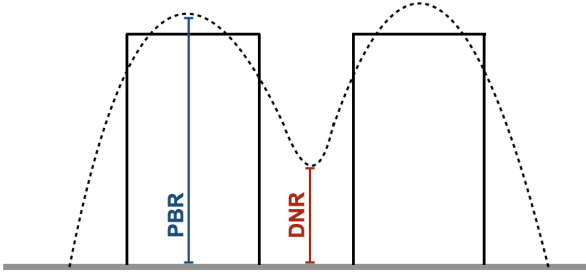Fig. 3. Sketch of a hypothetical reference (continuous line) and measured (dotted line) profile to clarify the meaning of the metrics PBD and DNR.

A. In particular, the singular value decomposition (SVD) is used to analyse the **A** matrices associated to the three MC cases, see Fig. 5, where the singular values are depicted using a semilog-y scale. One can note that MC1 penalizes higher-order eigenvalues; while MC3 does not significantly affect them. The discrete forward problem used to generate the measured profile (see eq. (2)) comes from a continuous Fredholm integral equation of the first kind with a smooth kernel. Hence, a low-pass measuring system is in place that, in discrete settings, results in an ill-determined rank system matrix **A**. Hence, its spectral analysis performed using the SVD results in a clustering of the smaller singular values towards the origin. This phenomenon is more pronounced in the MC1 case; while there is a negligible clustering in the MC3 case. This means that the MC1 scenario is the most challenging in terms of the ill-conditioning (condition number equal to 6248.18) of the system matrix. In fact, it represents a measurement configuration where a large aperture function (i.e., a strong low-pass filter) is used. The MC3 scenario results in the best conditioned problem (condition number equal to 2.79), since it comes from a continuous forward problem that calls for a narrower aperture function (i.e., a weaker low-pass filtering). Hence, regularisation is a mandatory choice in the MC1 case when dealing with the inverse problem; while its effects are almost negligible in the MC3 case. This justifies the behaviour of LW-P that results in an added-value with respect to LW in the MC2 cases; while it does not improve reconstruction's performance in MC3. It is also worth noting that, in the MC3 case, even the LW method does not improve significantly the conventional linear interpolation.

TABLE I
IF VALUES RELATED TO THE CONFIGURATIONS MC1, MC2 AND MC3
WHEN USING LW AND LW-P.

	LW-NP	LW-P
MC1	1.09	1.57
MC2	1.11	1.81
MC3	1.18	1.08

The second experiment refers to two 300 K narrow (50 samples) pulse functions separated by Δ (samples): 50, 20 and 10 (see Fig. 6 (a), (b) and (c), respectively). The reconstructed profiles using LW and LW-P are depicted in Fig. 7 that is arranged in a matrix format with the rows standing for
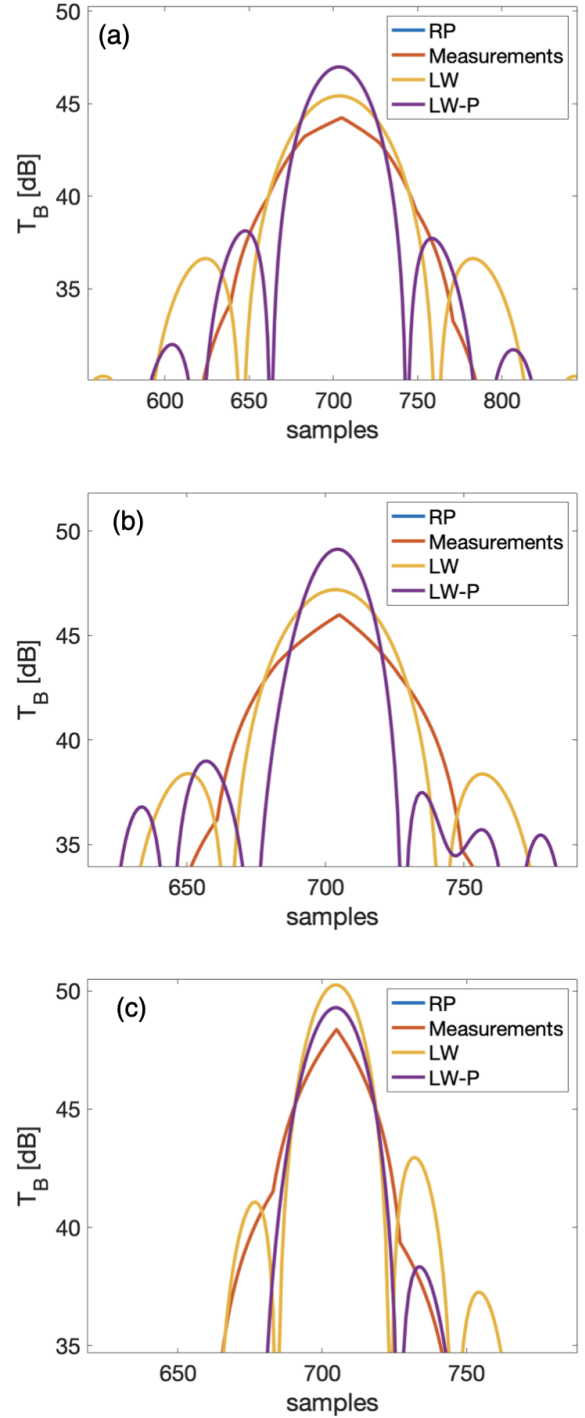

Fig. 4. Reconstruction of the 1-pixel Dirac-like delta function using both LW and LW-P for the scenario MC1 (a), MC2 (b) and MC3 (c). The noisy measurements, interpolated onto the finer-resolution grid, are also annotated. Note that dB scale is used.

the reference profiles depicted in Fig. 6 (a), (b) and (c), respectively. In this experiment, the LW-P method is run with $\alpha = 3$, while the LW method is approximated using $\alpha = 10^{-2}$. The three columns refer to the scenarios MC1, MC2 and MC3, respectively. In all the panels, the measured profile interpolated onto the finer resolution grid is also shown together with a horizontal bar showing the brightness temperature level of
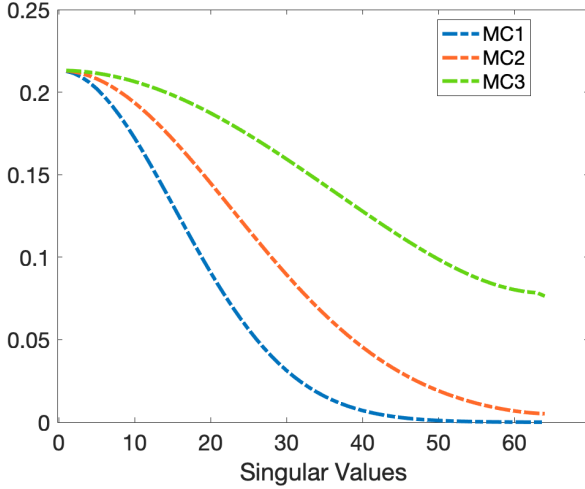
Fig. 5. Singular values associated to the three system functions describing the measurements process in the scenarios MC1, MC2 and MC3. Note that semiology-y scale is used.

the RP. Note that dB scale is adopted. When dealing with the MC1 scenario (see the first column), although both LW and LW-P succeed in reconstructing a profile sharper than the measured one, the LW-P method outperforms the LW one since it results in a reduction of the over-smoothing and, therefore, it reconstructs sharper edges. In fact, it provides a better reconstruction of the abrupt discontinuities in the region bounded by the two pulse functions. To analyse the separability in an objective way, a -3 dB threshold, evaluated with respect to RP, is considered (see dotted blue line in Fig. 7). Hence, the reconstructed pulse functions are separated when two distinguishable peaks are above the threshold. This means that, when $\Delta = 50$ (see first row) the two pulse functions are distinguishable in both the measurements and the reconstructions; while in the $\Delta = 20$ and $\Delta = 10$ samples (see second and third rows, respectively), the RP cannot be separated neither in the measurements, nor in the reconstructions. However, it can also be noted that the LW-P method is able to provide non-negligible distinguishable hints of signal associated to the two pulse functions in the $\Delta = 20$ case, while this is no longer true when LW is used. Hence, LW is never able to reach the performance of LW-P.

When dealing with the MC2 case, although LW-P still outperforms LW, the difference in their reconstructed profiles reduces significantly if compared to the MC1 case. LW-P allows distinguishing the two profiles correctly when $\Delta = 50$ and $\Delta = 20$; while non-negligible hints of signal belonging to the two pulse functions can be observed in the $\Delta = 10$ case. The LW method correctly distinguishes the two pulse functions only in the $\Delta = 50$ and $\Delta = 20$ cases; while almost negligible hints of signals are visible in the $\Delta = 10$ case. When dealing with the MC3 case, the intrinsic MWR spatial resolution is finer enough to make the pulse functions well distinguishable in the profiles measured at both $\Delta = 50$ and $\Delta = 20$ cases. In fact, the reconstructions practically do not improve the measurements when dealing with $\Delta = 50$ case; while they result in non-negligible improvements when

dealing with the $\Delta = 20$ and $\Delta = 10$ cases. In the $\Delta = 20$ case, LW-P results in a reconstructed profile that well-fits the RP in terms of the brightness level on the top of the pulse functions. The same applies also for the $\Delta = 10$ case. In addition, in both cases, LW-P outperforms LW, that results in an overestimated brightness temperature level. When dealing with separability of the two pulse functions, in the $\Delta = 20$ case the two RPs are distinguishable (according to the -3 dB threshold) in the measurements; while they are no longer distinguishable in the measured profile at $\Delta = 10$. The LW improves the separability in both the $\Delta = 20$ and $\Delta = 10$ cases with respect to the measured profile, and the LW-P. In the $\Delta = 10$ case, both the LW and the LW-P reconstructions show well-distinguishable hints of signals belonging to the two pulse functions. To deeply analyse the separability of the two pulse functions the DNR metric is evaluated, see Table II. Quantitative results confirm the qualitative analysis of Fig. 7. In general, the methods improve the measured profiles in terms of DNR. The LW-P method generally outperforms LW. The improvement is largest in the MC1 case when $\Delta = 50$. In the MC2 and MC3 cases, the finer intrinsic MWR spatial resolution reduces the difference between DNR values resulting from LW and LW-P. In some cases (MC2, $\Delta = 50$; MC3, $\Delta = 20$), LW outperforms LW-P. In the MC3 case, when $\Delta = 50$, the linearly interpolated measurements outperform the reconstructed profiles in terms of DNR.

The third experiment consists of discussing the performance of the reconstructions obtained by varying the amount of regularization jointly using the metrics IF, noise amplification and PBR, see Table III . The RP consists of a 300 K pulse function of 50 samples width, see Fig. 8 (a). The analysis consists of using the LW-P with different α values that include the one that best fits the LW behaviour. The scatter plots of Fig. 8 (b) and (c) depict the reconstruction's performance in terms of noise amplification and IF related to the MC1 and MC3 cases, respectively. The reconstructions obtained using LW-P with the 5 filter's values are labeled as LW-P$_{f1}$ up to LW-P$_{f5}$ with the former one calling for a performance very close to the LW one. The metric noise amplification is evaluated by averaging the absolute value of the RMSE related to the shaded boxes depicted in Fig. 8 (a). Note that the α values shown in Fig. 8 (b) and (c) are normalised to LW-P$_{f1}$. When dealing with the MC1 case, see Fig. 8 (b), the performance of LW-P is always superior to the LW one in terms of IF and PBR for all the α values. The largest IF (~ 1.5) and PBR (0.998) values are obtained in the LW-P $_{f5}$ case with an α value equal to 0.005. The lowest IF and PBR values (larger than the the LW ones) are achieved in the LW-P $_{f1}$ case (~ 1.1 and 0.791, respectively) with an α value equal to 0.5, see Table III where non-normalised α values are listed together with the metric PBR. When dealing with the noise amplification, the superior performance of LW-P can ben noted at the expense of a noise amplification always larger than the LW one. In details, LW-P$_{f1}$, LW-P$_{f2}$ and LW-P$_{f3}$ improve the IF performance with respect to LW, while keeping the noise amplification at levels comparable with the ones achieved by LW. When using LW-P$_{f4}$ and LW-P$_{f5}$ the slight improvement in IF performance is achieved at the expense of a larger increase of the noise

TABLE II
DNR METRIC EVALUATED USING THE MEASUREMENTS AND THE RECONSTRUCTIONS RELATED TO THE SCENARIOS MC1, MC2 AND MC3 THAT REFER TO THE REFERENCE PROFILES DEPICTED IN FIG. 6.

Δ (samples)	50			20			10		
	Measurements	LW	LW-P	Measurements	LW	LW-P	Measurements	LW	LW-P
MC1	121.55	95.38	0.88	211.82	241.11	181.32	244.08	292.51	257.55
MC2	69.15	9.81	35.45	192.21	162.69	81.70	245.41	243.62	180.86
MC3	15.44	38.74	22.60	128.21	32.77	75.76	212.62	160.30	180.18

TABLE III
IF, NOISE AMPLIFICATION AND PBR VALUES RELATED TO THE RP OF FIG. 8 AND OBTAINED USING LW AND LW-P. THE LATTER IS RUN WITH DIFFERENT FILTER'S VALUES.

MC1				
	Filter	IF	Noise Amplification	PBR
LW	-	1.11	0.5119	0.791
LW-P$_{f1}$	0.5	1.18	0.5449	0.816
LW-P$_{f2}$	0.1	1.35	1.3821	0.927
LW-P$_{f3}$	0.05	1.39	1.988	0.946
LW-P$_{f4}$	0.01	1.4	4.249	0.969
LW-P$_{f5}$	0.005	1.49	8.2959	0.998
MC3				
	Filter	IF	Noise Amplification	PBR
LW	-	1.08	1.4282	0.879
LW-P$_{f1}$	2	1.08	0.9693	0.899
LW-P$_{f2}$	3	1.06	0.6377	0.944
LW-P$_{f3}$	4	1.04	0.2903	0.998
LW-P$_{f4}$	5	1.02	0.2798	0.942
LW-P$_{f5}$	6	1.01	0.2251	0.885

amplification. A fair compromise between noise amplification and resolution enhancement is achieved in the LW-P$_{f3}$ case, with a noise amplification ~ 2 and an improvement factor IF $= 1.4$. With respect to the MC3 case, see Fig. 8 (c), the finer intrinsic spatial resolution and the lower overlapping among adjacent beams limit the performance of both LW and LW-P that result in IF values close to the unity and a reduced noise amplification with respect to the MC1 case, see Table III. The reduced noise amplification is likely due to the filtering effects of the preconditioner. Hence, this confirms that the antenna pattern deconvolution is not needed in the MC3 case.

B. Real measurements

Experiments on actual measurements refer to the brightness temperature profiles extracted from data collected by the Special Sensor Microwave Images (SSM/I) radiometer that flown abroad the United States Defense Meteorological Satellite Program. SSM/I is a multi-channel MWR and, for the purposes of this study, measurements collected in 1988 by the lowest spatial resolution channel, i.e., the 19.35 GHz channel, and the 37.00 GHz channel are considered since they match the parameters related to MC1 and MC3, respectively. In fact, the 19.35 GHz measurements call for an along-scan spatial resolution of 43 km whilst in the 37.0 GHz case the latter is 29 km. In both the channels the radiometer, whose orbital altitude is 833 km with a nominal swath width of 1400 km, performs 64 uniformly spaced (25 km) measurements along the along-scan direction.

The fourth experiment refers to radiometer measurements collected over the Canary islands, see Fig. 9. The figure is arranged in a matrix format, with the two columns (a,c,e) and (b,d,f) standing for 19.35 GHz and 37.0 GHz H-polarized channel, respectively. The rows are related to: the brightness temperature field measured by the SSM/I (first row); the profile measured along with the white transect of panel (a) (second row) and the reconstructions obtained using LW and LW-P together with the linearly interpolated measurements (third row). When dealing with the 19.35 GHz case (see Fig. 9 (a)), both LW and LW-P provide reconstructed profiles sharper than the measurements (see Fig.9 (e)). The LW-P is run with $\alpha = 0.2$ while the LW is approximated by $\alpha = 0.05$. The profile reconstructed using LW-P improves the measurements in terms of both reconstruction of the brightness temperatuere level of the small islands, and in the separation among them. The reconstructed profile using LW, although correctly follows the profile of the small islands, results in overestimations and underestimations. The performance of both LW-P and LW are similar when dealing with the continental area depicted in the right-hand-most part of the image. When dealing with the 37.00 GHz case (see Fig. 9 (f)) the two methods result in similar reconstruction performance with LW-P calling for lower fluctuations than LW. As far as for the simulated scenario, even in this case the fine native SSM/I spatial resolution and the very low level of overlapping among adjacent beams let the reconstructed profiles being very close to the measured one.

The fifth experiment is related to radiometer measurements collected over an area that includes part of the United Kingdom, Ireland, Northern Europe and the Scandinavian Peninsula, see Fig. 10 that is arranged in a fashion similar to Fig. 9. This experiment aims at analysing the performance of the two methods when reconstructing small islands. On this purpose, a transect (see dotted white line) is considered that includes the isle of Man, see red circle in Fig. 10 (c,d). The profiles reconstructed using LW and LW-P are depicted together with the measured profile interpolated on the finer resolution grid, see Fig. 10 (e) and (f) for the 19.35 GHz and the 37 GHz cases, respectively. The LW-P is run with $\alpha = 0.2$ while the LW is approximated by $\alpha = 0.09$. When dealing with the 19.35 GHz case (Fig. 10 (e)), both LW and LW-P result in a reconstructed profile sharper than the measured one although characterised by Gibbs-related fluctuations. The LW-P reconstruction performs best, since it sharpens the edges resulting in a better reconstructed isle of Man. When dealing with the 37.00 GHz case (see Fig. 10 (f)) the two methods result in almost similar performance that does
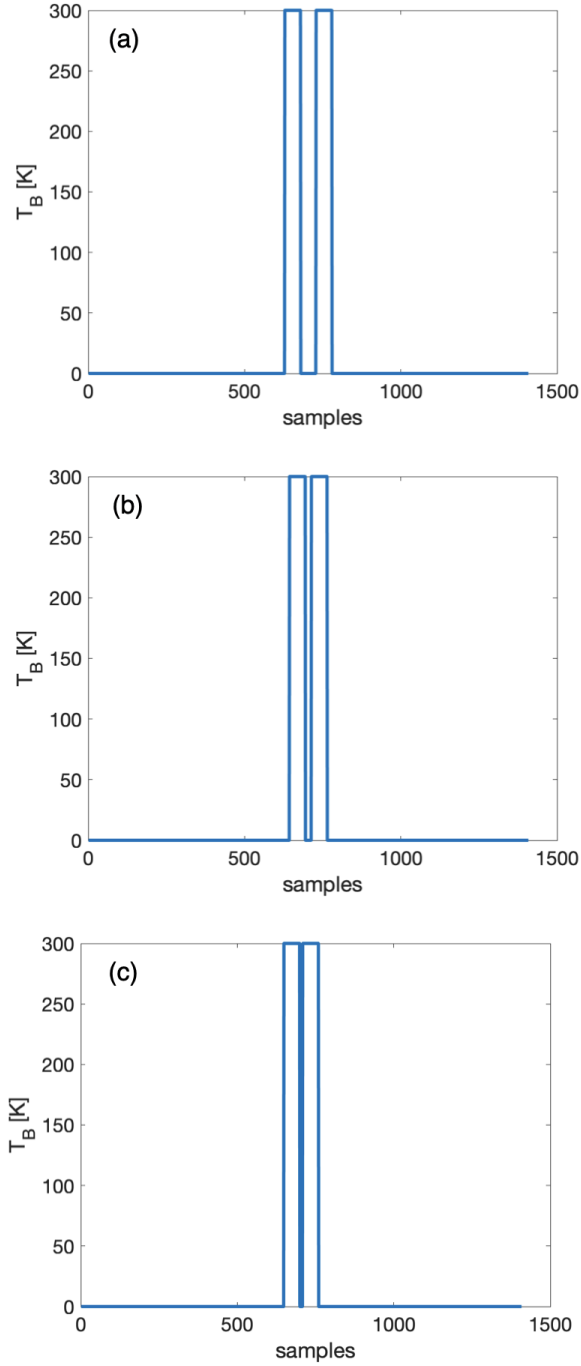
Fig. 6. Three RPs that consist of pulse functions calling for a 300 K brightness temperature and different separations (Δ): $\Delta = 50$ samples (a); $\Delta = 20$ samples (b) and $\Delta = 10$ samples (c).

TABLE IV
IF, NOISE AMPLIFICATION AND PBR VALUES RELATED TO THE RP OF FIG. 11 AND OBTAINED USING LW AND LW-P. THE LATTER IS RUN WITH DIFFERENT FILTER'S VALUES.

	19.35 GHz		
	Filter	IF	Noise Amplification
LW	-	1.24	0.6025
LW-P$_{f1}$	1	1.35	0.5540
LW-P$_{f2}$	0.5	1.74	0.5971
LW-P$_{f3}$	0.2	2.1	1.0814
LW-P$_{f4}$	0.15	2.22	1.2973
LW-P$_{f5}$	0.1	2.34	1.5561
	37.00 GHz		
	Filter	IF	Noise Amplification
LW	-	2.21	1.0572
LW-P$_{f1}$	1	2.5	1.6468
LW-P$_{f2}$	0.5	2.78	2.4361
LW-P$_{f3}$	0.2	3.75	5.0583
LW-P$_{f4}$	0.15	4.17	6.6008
LW-P$_{f5}$	0.1	5	9.7575

and (b) for the 19.35 GHz and 37.00 GHz cases, respectively, where the same format of Fig. 8 is adopted. When dealing with the 19.35 GHz case (see Fig. 11 (a)), LW-P always outperforms LW in terms of IF with the largest IF (2.34) being achieved with a filter equal to 0.1 (LW-P$_{f5}$). The lowest IF value (1.35) is achieved with the filter value 1 (LW-P$_{f1}$), see Table IV, and it is slightly higher than the corresponding LW IF value (1.24). With respect to noise amplification, it can be noted that up to LW-P$_{f2}$, the superior performance of LW-P is not achieved at the expense of a larger noise amplification. In particular, the latter is indeed a bit lower than the LW case. From LW-P $_{f3}$ onwards, the superior performance of LW-P calls for a noise amplification larger than the LW one. When dealing with the 37.00 GHz case, see Fig. 11 (b), the joint analysis of IF and noise amplification confirms that in this case the reconstruction algorithm is generating very noisy reconstructions at low α values. This confirms that in this scenario (finer intrinsic spatial resolution and low overlapping among adjacent beams) antenna pattern deconvolution algorithms do not work properly.

CONCLUSIONS

A study on the ability of enhancing of the spatial resolution of conical-scanning microwave radiometer brightness profiles using an iterative regularizing antenna pattern deconvolution method that allows tuning the level of regularization is presented. The enhancement capabilities are discussed against the overlapping among adjacent beams and native spatial resolution using both simulated and actual radiometer measurements. In particular, three MRFs that resemble three conical scanning radiometer's measurement configurations and measured 1D profiles extracted from data collected by the SSM/I sensor are considered.

When retrieving the brightness profile on a finer spatial resolution grid inverting the linear ill-posed forward problem, special attention is due to ill-conditioning of the problem that jointly depends on intrinsic radiometer spatial resolution and the overlapping among adjacent beams. In case of finer spatial resolution radiometer measurements calling for a lower overlapping among adjacent beams, regularization is not a key

not improve significantly the measured profile. However, LW-P results in a better reconstructed island with respect to LW. To quantitatively discuss the reconstruction's performance, the metrics IF (referred to the isle of Man) and noise amplification are used. Note that since in this case the RP is not available, the metric PBR cannot be evaluated. In addition, to evaluate IF a threshold equal to - 1 dB is used since the brightness temperature level is not strong enough to allow using a threshold equal to -3 dB. Results are depicted in Fig. 11 (a)
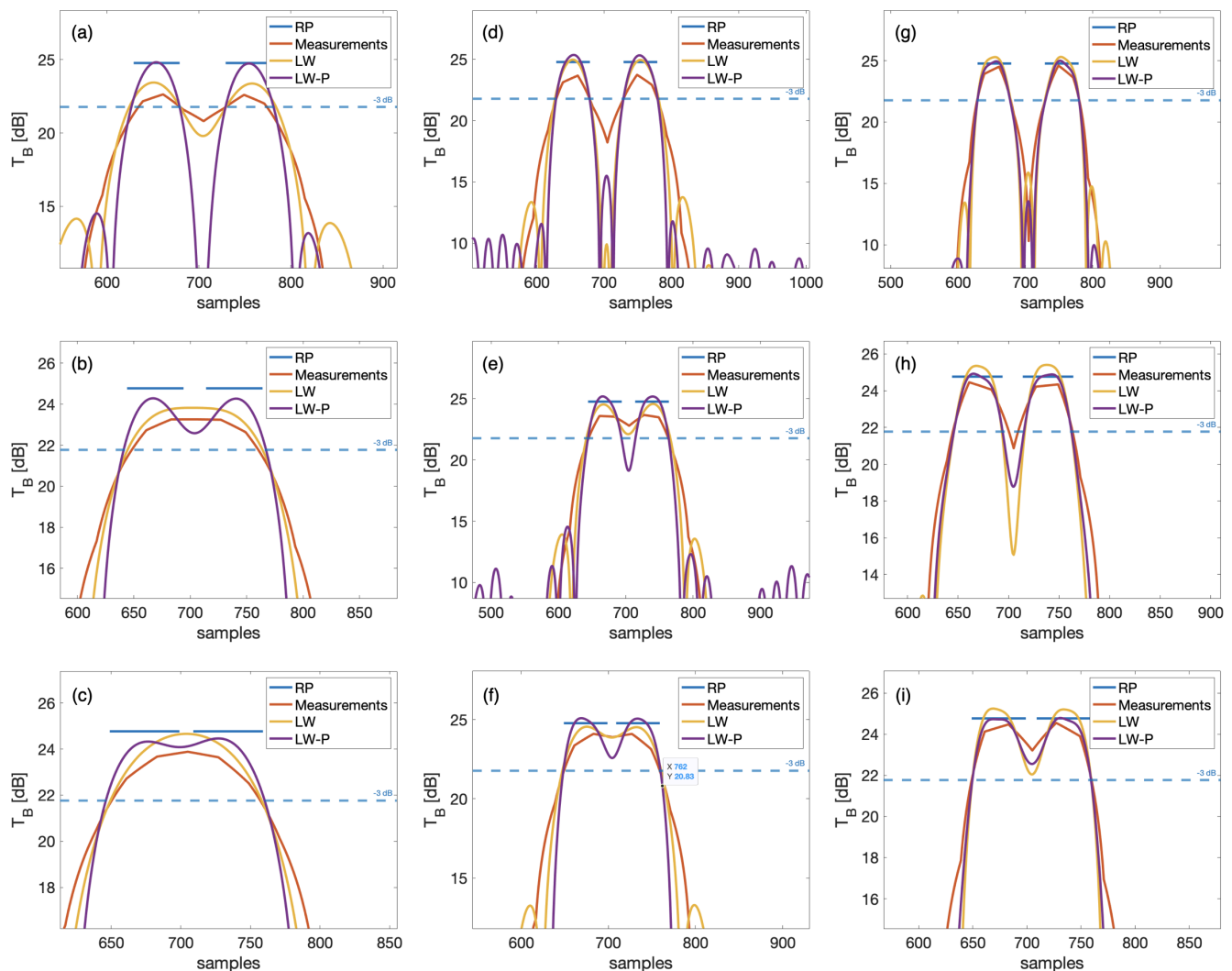
Fig. 7. Profiles reconstructed using LW and LW-P. The rows (a,d,g), (b,e,h) and (c,f,i) refer to the reconstructions of the RPs depicted in Figure 6 (a), (b) and (c), respectively. The columns (a,b,c), (b,e,f) and (g,h,i) refer to the MC1, MC2 and MC3 cases, respectively. In all the panels, the measured profile, interpolated onto the finer-resolution grid is also shown together with horizontal bars that stand for the brightness level on the top of the RP. The dotted blue line depict the -3 dB threshold. Note that dB scale is used.

issue to be dealt with. When dealing with lower-resolution measurements resulting in higher overlapping among adjacent beams, regularization plays a key role. In this latter case a proper tuning of the regularization parameter allows an application-oriented reconstruction calling for a desired trade-off between enhanced performance and noise amplification.

The analysis carried on both synthetic and actual radiometer measurements that resemble the SSM/I configuration shows that:

- when dealing with the 19.35 GHz channel - i.e., the one that best matches the simulated low-resolution high-overlapping MC1 configuration - the improvement of the spatial resolution can reach up to 2.34 at the expense of a noise amplification equal to 1.56. In addition, to reach an enhancement of 1.64 the noise amplification is less than 0.6.
- when dealing with the 37.0 GHz channel - i.e., the one that best matches the simulated high-resolution low-

overlapping MC3 configuration - the improvement of the spatial resolution is negligible and it is actually obtained at the expense of an intolerable noise amplification.

REFERENCES

[1] F. T. Ulaby, D. G. Long, W. J. Blackwell, C. Elachi, A. K. Fung, C. Ruf, K. Sarabandi, H. A. Zebker, and J. Van Zyl, *Microwave Radar and Radiometric Remote Sensing*. University of Michigan Press, 2014. [Online]. Available: https://books.google.it/books?id=y6pZngEACAAJ

[2] D. G. Long and M. J. Brodzik, "Optimum Image Formation for Spaceborne Microwave Radiometer Products," *IEEE Transactions on Geoscience and Remote Sensing*, vol. 54, no. 5, pp. 2763–2779, may 2016. [Online]. Available: http://ieeexplore.ieee.org/document/7366582/

[3] F. Lenti, F. Nunziata, C. Estatico, and M. Migliaccio, "Analysis of Reconstructions Obtained Solving lp-Penalized Minimization Problems," *IEEE Transactions on Geoscience and Remote Sensing*, vol. 53, no. 9, pp. 4876–4886, sep 2015. [Online]. Available: http://ieeexplore.ieee.org/document/7084656/

[4] F. Lenti, F. Nunziata, M. Migliaccio, and G. Rodriguez, "Two-Dimensional TSVD to Enhance the Spatial Resolution of Radiometer Data," *IEEE Transactions on Geoscience and Remote Sensing*, vol. 52, no. 5, pp. 2450–2458, 2014.
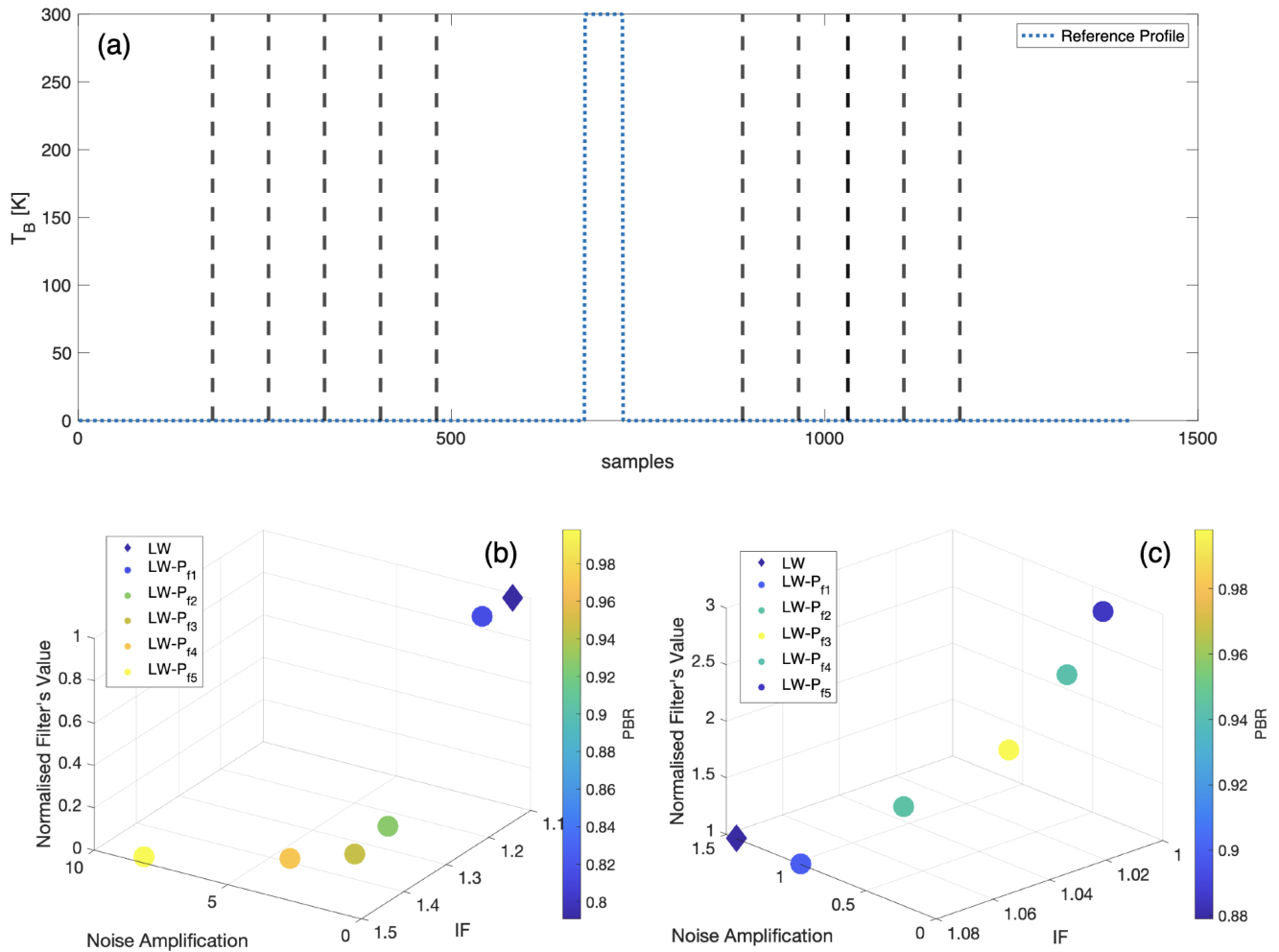
Fig. 8. Reconstructions of a RP that consists of a 300 K narrow (50 samples) pulse function located at the center of the profile (a). The three-dimensional scatter plots contrast the metrics IF, noise amplification and PBR for different values of the preconditioner filter for the scenarios MC1 (b) and MC3 (c). The circles are coloured according to the PBR level.

[5] D. G. Long and D. L. Daum, "Spatial resolution enhancement of SSM/I data," *IEEE Transactions on Geoscience and Remote Sensing*, vol. 36, no. 2, pp. 407–417, mar 1998.

[6] EOSDIS, "Data Processing Levels." [Online]. Available: https://science.nasa.gov/earth-science/earth-science-data/data-processing-levels-for-eosdis-data-products

[7] M. J. Brodzik, B. Billingsley, T. Haran, B. Raup, and M. H. Savoie, "EASE-Grid 2.0: Incremental but Significant Improvements for Earth-Gridded Data Sets," *ISPRS International Journal of Geo-Information*, vol. 1, no. 1, pp. 32–45, mar 2012. [Online]. Available: http://www.mdpi.com/2220-9964/1/1/32

[8] M. Brodzik, B. Billingsley, T. Haran, B. Raup, and M. Savoie, "Correction: Brodzik, M.J., et al. EASE-Grid 2.0: Incremental but Significant Improvements for Earth-Gridded Data Sets. ISPRS International Journal of Geo-Information 2012, 1, 32–45," *ISPRS International Journal of Geo-Information*, vol. 3, no. 3, pp. 1154–1156, sep 2014. [Online]. Available: http://www.mdpi.com/2220-9964/3/3/1154

[9] F. Wentz, "SSM/I Version-7 Calibration Report," 2013.

[10] M. J. Brodzik and D. Long, "Calibrated Passive Microwave Daily EASE Grid 2.0 Brightness Temperature ESDR (CETB)," *NASA MEaSUREs*, 2015.

[11] K. W. Knowles, E. J. Njoku, R. L. Armstrong and M. J. Brodzik, "Nimbus-7 SMMR Pathfinder Daily EASE-Grid Brightness Temperature," 2000. [Online]. Available: http://nsidc.org/data/nsidc-0071

[12] K. Knowles, M. Savoie, R. Armstrong, and M. J. Brodzik, "AMSR-E/Aqua daily EASE-grid brightness temperatures," *Digital media*, 2006.

[13] J. Maslanik and J. Stroeve, "DMSP SSM/I-SSMIS Daily Polar Gridded Brightness Temperatures, Version 4," 2004. [Online]. Available: https://nsidc.org/data/nsidc-0001

[14] P. Hansen, *Rank-Deficient and Discrete Ill-Posed Problems*. Society for Industrial and Applied Mathematics, 1998. [Online]. Available: http://epubs.siam.org/doi/abs/10.1137/1.9780898719697

[15] M. Migliaccio and A. Gambardella, "Microwave radiometer spatial resolution enhancement," *IEEE Transactions on Geoscience and Remote, Sensing*, vol. 43, 2005.

[16] F. Lenti, F. Nunziata, C. Estatico, and M. Migliaccio, "On the Spatial Resolution Enhancement of Microwave Radiometer Data in Banach Spaces," *IEEE Transactions on Geoscience and Remote Sensing*, vol. 52, no. 3, pp. 1834–1842, mar 2014. [Online]. Available: http://ieeexplore.ieee.org/document/6517236/

[17] ——, "Conjugate Gradient Method in Hilbert and Banach Spaces to Enhance the Spatial Resolution of Radiometer Data," *IEEE Transactions on Geoscience and Remote Sensing*, vol. 54, no. 1, pp. 397–406, 2016.

[18] M. Alparone, F. Nunziata, C. Estatico, and M. Migliaccio, "On the Use of Preconditioners to Improve the Accuracy and Effectiveness of Iterative Methods to Enhance the Spatial Resolution of Radiometer Measurements," *IEEE Geoscience and Remote Sensing Letters*, pp. 1–5, 2020. [Online]. Available: https://ieeexplore.ieee.org/document/9050438/

[19] ——, "A Multichannel Data Fusion Method to Enhance the Spatial Resolution of Microwave Radiometer Measurements," *IEEE*
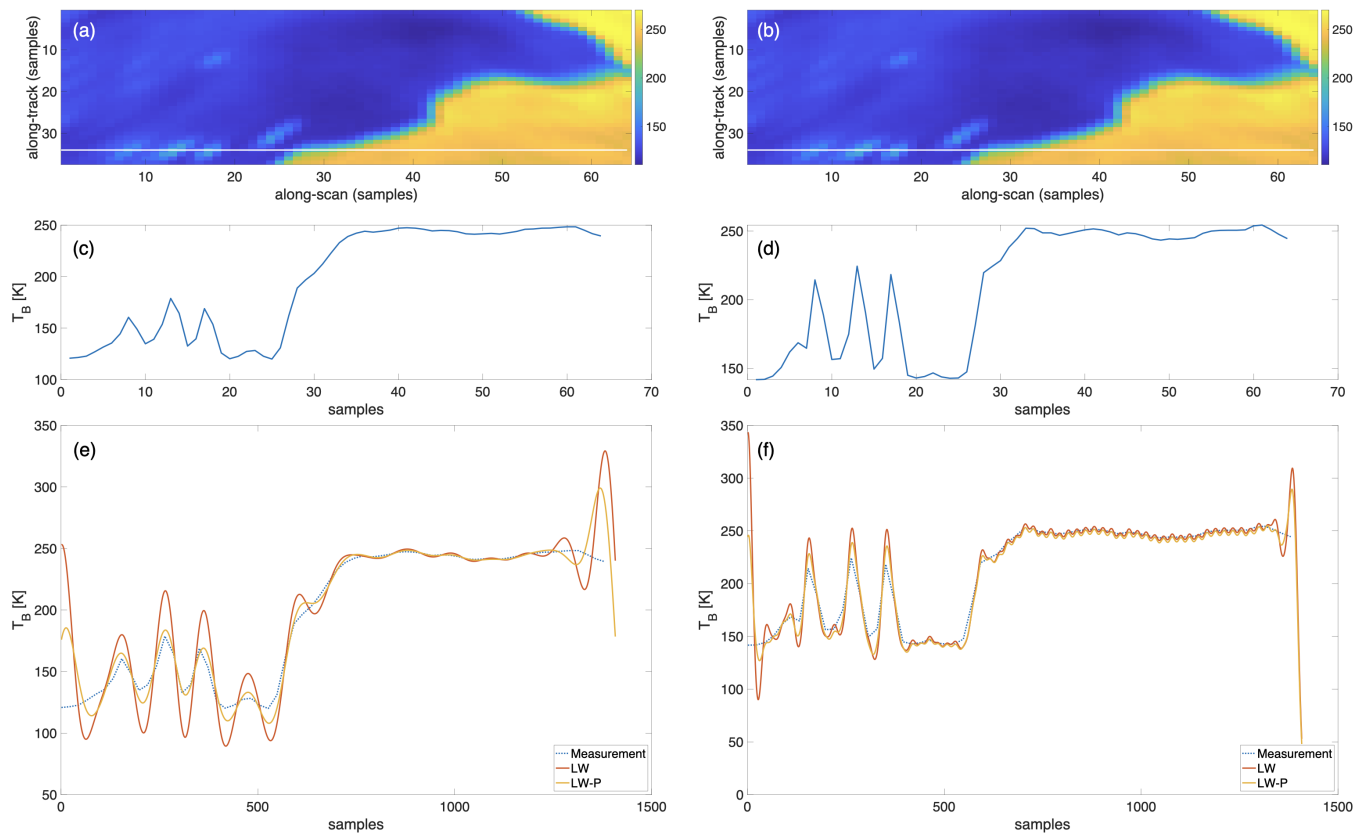
Fig. 9. Brightness field collected by the SSM/I over the Canary islands in 1988. The first column refers to the measurement and the processing related to the 19.35 GHz channel; while the second column refers to the 37.0 GHz channel. The brightness profile measured along the transects shown as white lines in (a) and (b) are depicted in (c) and (d) for the 19.35 GHz and the 37.0 GHz cases, respectively. The linearly interpolated measurements and the reconstructions obtained using both LW and LW-P are depicted in (e), (f) for the 19.35 GHz and the 37.00 GHz case, respectively.

Transactions on Geoscience and Remote Sensing, pp. 1–9, 2020. [Online]. Available: https://ieeexplore.ieee.org/document/9134973/

[20] F. Lenti, F. Nunziata, C. Estatico, and M. Migliaccio, "Spatial Resolution Enhancement of Earth Observation Products Using an Acceleration Technique for Iterative Methods," *IEEE Geoscience and Remote Sensing Letters*, vol. 12, no. 2, pp. 269–273, feb 2015. [Online]. Available: http://ieeexplore.ieee.org/lpdocs/epic03/wrapper.htm?arnumber=6861444

[21] M. Alparone, F. Nunziata, C. Estatico, and M. Migliaccio, "On the Use of Preconditioners to Improve the Accuracy and Effectiveness of Iterative Methods to Enhance the Spatial Resolution of Radiometer Measurements," *IEEE Geoscience and Remote Sensing Letters*, pp. 1–5, 2020.

[22] D. G. Long, P. J. Hardin, and P. T. Whiting, "Resolution enhancement of spaceborne scatterometer data," *IEEE Transactions on Geoscience and Remote Sensing*, vol. 31, no. 3, pp. 700–715, 1993.

[23] D. G. Long, M. J. Brodzik, and M. A. Hardman, "Enhanced-Resolution SMAP Brightness Temperature Image Products," *IEEE Transactions on Geoscience and Remote Sensing*, vol. 57, no. 7, pp. 4151–4163, jul 2019.

[24] C. Estatico, E. Ngondiep, S. Serra-Capizzano, and D. Sesana, "A note on the (regularizing) preconditioning of g-Toeplitz sequences via g-circulants," *Journal of Computational and Applied Mathematics*, vol. 236, no. 8, pp. 2090–2111, 2012. [Online]. Available: http://www.sciencedirect.com/science/article/pii/S0377042711005127

[25] C. Garoni and S. Serra-Capizzano, *Generalized Locally Toeplitz sequences: theory and applications*. Springer, 2017, vol. 1.

[26] C. Estatico, "A Class of Filtering Superoptimal Preconditioners for Highly Ill-Conditioned Linear Systems," *BIT Numerical Mathematics*, vol. 42, no. 4, pp. 753–778, 2002. [Online]. Available: https://doi.org/10.1023/A:1021948319714

[27] ——, "A classification scheme for regularizing preconditioners, with application to Toeplitz systems," *Linear Algebra and its Applications*, vol. 397, pp. 107–131, 2005. [Online]. Available: http://www.sciencedirect.com/science/article/pii/S002437950400446X

[28] G. Strang, "A Proposal for Toeplitz Matrix Calculations," *Studies in Applied Mathematics*, vol. 74, no. 2, pp. 171–176, apr 1986. [Online]. Available: https://doi.org/10.1002/sapm1986742171

[29] C. Estatico, "Regularization Processes for Real Functions and Ill-posed Toeplitz Problems," in *Recent Advances in Operator Theory and its Applications*. Basel: Birkhäuser Basel, 2005, pp. 161–178.
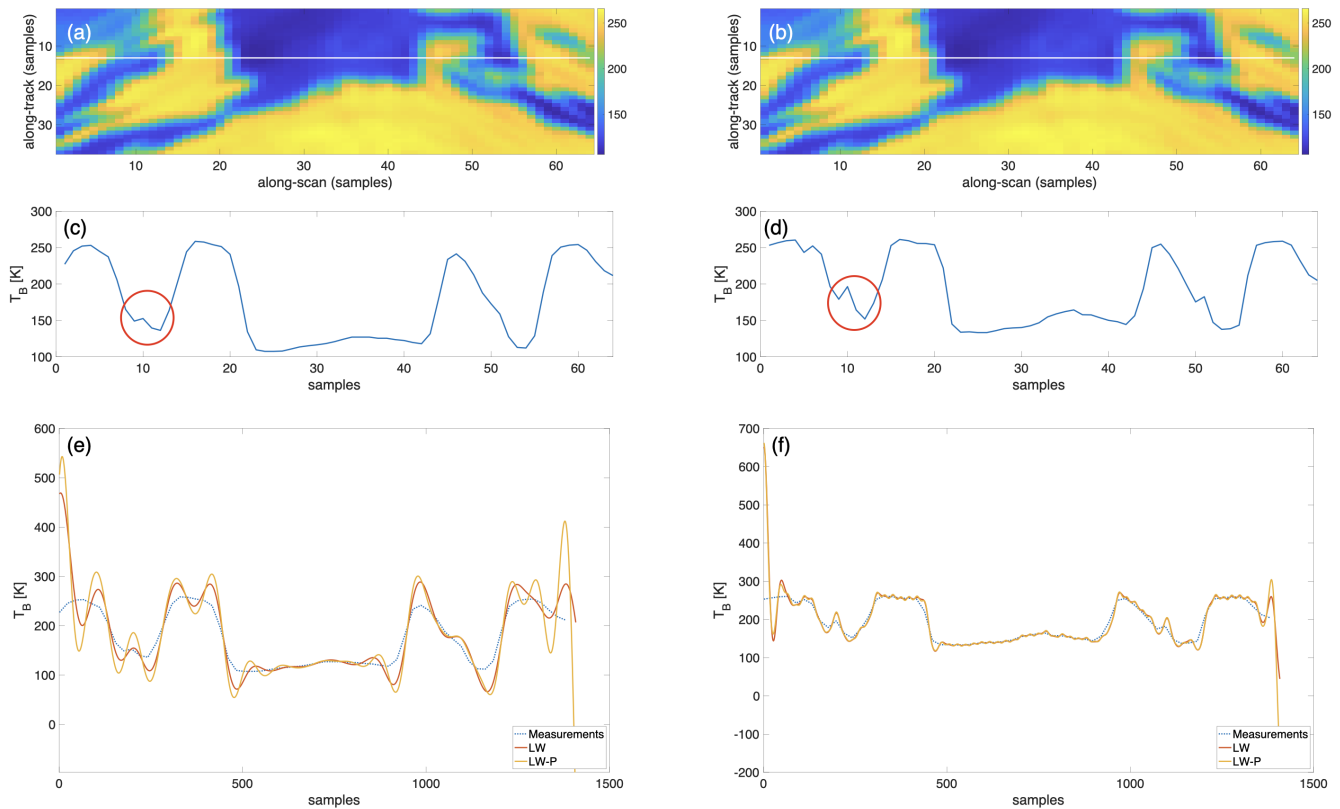
Fig. 10. Brightness field collected by the SSM/I over part of the United Kingdom, Ireland, Northern Europe and the Scandinavian Peninsula in 1988. The first column refers to the measurement and the processing related to the 19.35 GHz channel; while the second column refers to the 37.0 GHz channel. The brightness profile measured along the transects (shown as white lines in (a) and (b)) over an area that includes the isle of Man are depicted in (c) and (d) for the 19.35 GHz and the 37.0 GHz cases, respectively. Note that the samples collected within the isle of Man are enclosed in the red circle. The linearly interpolated measurements and the reconstructions obtained using both LW and LW-P are depicted in (e), (f) for the 19.35 GHz and the 37.00 GHz case, respectively.
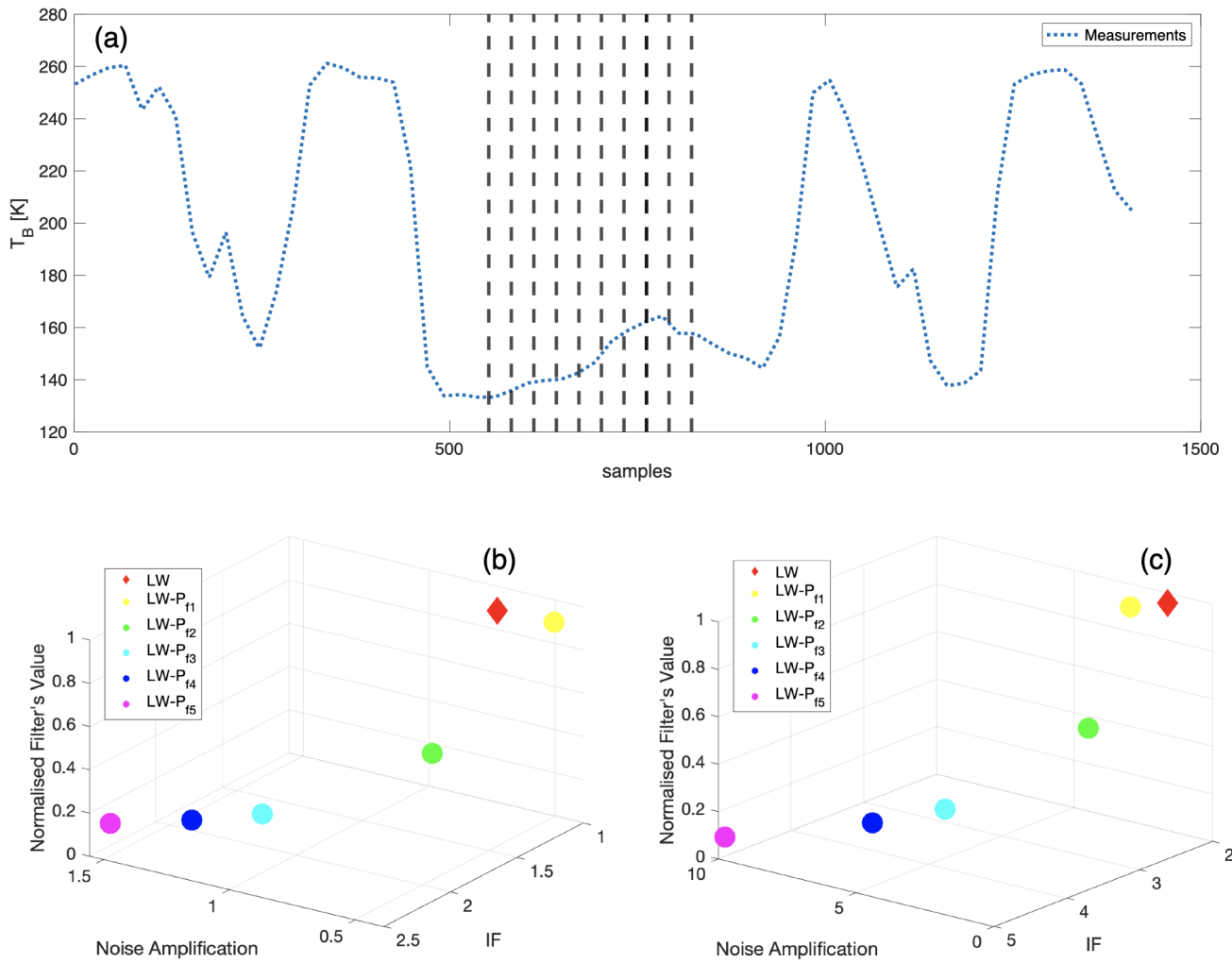
Fig. 11. Reconstructions related to the actual SSM/I radiometer profile depicted in Fig. 10. The measured profile interpolated onto the finer resolution grid is depicted in the panel (a) where the shaded boxes that are used to evaluate noise amplification are also annotated. The three-dimensional scatter plots contrast the metrics IF and noise amplification for different values of the preconditioner filter for the 19.35 GHz (b) and 37.00 GHz (c) cases.